A Simple and Versatile Hollow MOFs Synthesis Strategy for CO_2 Separation and Catalysis

Yanhua Shao[#a], Jie Xu[#a], Ze-Xian Low[b], Chunhong Chen[c], Hong Jiang[*a], Rizhi Chen[*a]

[a] State Key Laboratory of Materials-Oriented Chemical Engineering, Nanjing Tech University, Nanjing 211816, Jiangsu, China.

[b] Department of Chemical Engineering, Monash University, Clayton, Victoria 3800, Australia.

[c] Department of Industrial and Systems Engineering, the Hong Kong Polytechnic University, Hung Hom, Hong Kong 999077, China.

[#] These authors contribute equally to this work.

[*] Corresponding authors: hjiang@njtech.edu.cn; rizhichen@njtech.edu.cn.

Experimental section

Chemicals: Zinc nitrate hexahydrate (Zn(NO$_3$)$_2$·6H$_2$O, 99%), cobalt nitrate hexahydrate (Co(NO$_3$)$_2$·6H$_2$O, 99%) and 2-methylimidazole (2-MeIM, 99%) were purchased from Sigma-Aldrich. Zinc nitrate monohydrate and anhydrous zinc nitrate were obtained by drying zinc nitrate hexahydrate in vacuum at 130 ºC. Palladium acetate (Pd(OAc)$_2$, 98%) was purchased from Sin-platinum Metals Co., Ltd., China. Methanol (99.9%) and acetone (99.8%) were supplied by Yonghua Chemical Co., Ltd., China. Ethanol (99.7%) was supplied by Yasheng Chemical Co., Ltd., China. 1-Propanol (99%) was supplied by Shanghai Macklin Chemical Reagent Co., Ltd., China. *p*-Benzenediol (99%), 1-butanol (99.5%), 1-octanol (99%), phenol (99%) and nitric acid (65~68%) were provided by Sinopharm Chemical Reagent Co., Ltd., China. 1-Pentanol (99%), 1-hexanol (99%), 1-heptanol (98%), 1-nonanol (98%), 1-decanol (98%), 1-hexene (99%), cyclohexene (99%), tetra-styrene (98%), *p*-nitrophenol (98%), *o*-nitrophenol (98%), *p*-nitrobenzoic acid (99%), *p*-nitrobenzaldehyde (97%), *p*-nitrotoluene (99%), 3-aminophenol, *o*-cresol (99%), *p*-cresol (99%) and *m*-cresol (99%) were obtained from Shanghai Aladdin Biochemical Technology Co., Ltd., China. Cyclohexane was purchased from Shanghai Shenbo Chemical Regent Co., Ltd., China. Cyclohexane (99.7%) and sodium borohydride (NaBH$_4$, 97%) was purchased from Shanghai Lingfeng Chemical Regent Co., Ltd., China. 1-naphthol and guaiacol were obtained from Shanghai Macklin Biochemical Co., Ltd., China. CO$_2$ (99.9 vol %), CH$_4$ (99.9 vol%), N$_2$ (99.9 vol%) and H$_2$ (99.9 vol%) were acquired from Nanjing Special Gas Factory Co., Ltd., China. All chemicals were used as received.

Synthesis of MOFs

Synthesis of HZIF-8: 2-MeIM (1.236 g) was dissolved in 50 mL of 1-octanol and added to Zn(NO$_3$)$_2$·6H$_2$O/1-octanol solution (10 mL, 7 g/L) under stirring at 30 °C for 5 min, and then kept undisturbed at 30 °C for 24 h. The resulting products were centrifuged and washed with methanol for 5 times, and then dried in a vacuum oven at 70 °C overnight.

Synthesis of SZIF-8: 2-MeIM (4.944 g) was dissolved in 50 mL of deionized water and added to Zn(NO$_3$)$_2$·6H$_2$O aqueous solution (50 mL, 28 g/L) under stirring at 30 °C for 5 min, and then kept undisturbed at 30 °C for 24 h. The resulting products were centrifuged and washed with methanol for 5 times, and then dried in a vacuum oven at 70 °C overnight.

Synthesis of HZnCo-ZIF: 2-MeIM (1.236 g) was dissolved in 50 mL of 1-octanol and added to 1-octanol solution (10 mL, containing 0.0342 g of Co(NO$_3$)$_2$·6H$_2$O and 0.035 g of Zn(NO$_3$)$_2$·6H$_2$O). After stirring for 5 min, the reaction solution was placed in a water bath and kept undisturbed at 30 °C for 24 h. Purple products were obtained by centrifugation and washed with methanol 5 times, and then dried in a vacuum oven at 70 °C overnight.

Synthesis of Pd@ZIF-8: The loading of the Pd nanoparticles with a calculated Pd content of 4.3 wt.% was achieved using the wet impregnation method. The support (0.1 g) was dispersed in a Pd(OAc)$_2$ methanol solution (20 mL, 0.5 g/L) and stirred at 30 °C for 3 h. Subsequently, the samples were collected by filtration, repeatedly washed with methanol until a colorless filtrate was obtained, and finally dried at 70 °C overnight. The corresponding catalysts were denoted as Pd@HZIF-8 and Pd@SZIF-8.

Synthesis of HZIF-67: Co(NO$_3$)$_2$·6H$_2$O (1.091 g) and 2-MeIM (19.704 g) were dissolved in 40 mL and 200 mL of n-octanol, respectively. The former was slowly added to the latter with stirring for 5 min and then kept undisturbed at 30 °C for 6 h. The products were collected by

centrifugation, washed with methanol for 5 times, and dried at 70 °C for 24 h. The obtained samples were recorded as HZIF-x-y, where x represents the amount of 2-MeIM in per L of 1-octanol (mol/L) and y represents the synthesis time (h).

Synthesis of HCNs: The as-prepared HZIFs were placed in a ceramic boat in pure Ar flow (60 mL/min) in a tube furnace. First, the samples were heated to 450 °C at a rate of 5 °C/min for 90 min. Then the temperature was further increased to 700 °C at a rate of 2 °C/min for 90 min. Finally, the furnace was allowed to cool to room temperature. The resulting samples were etched with nitric acid solution (30%) by reflux at 60 °C for 3 h. Subsequently, the samples were collected by filtration, repeatedly washed with deionized water until a colorless filtrate was obtained, and finally dried at 70 °C overnight. The products were named as HCN-x-y.

Synthesis of Pd@HCNs: The loading of the Pd nanoparticles with a calculated Pd content of 2 wt.% was achieved using the wet impregnation method. The support (0.15 g) was dispersed in a Pd(OAc)$_2$ acetone solution (15 mL, 0.42 g/L) and stirred at 30 °C for 12 h. Subsequently, the resulting samples were rotary evaporated and dried at 70 °C overnight. Finally, the prepared materials were reduced in H$_2$ in a pipe furnace at 250 °C for 300 min. The corresponding catalysts were denoted as Pd@HCN-x-y.

Characterization

High-resolution transmission electron microscopy (HRTEM, Talos-F200X) and field emission scanning electron microscopy (FESEM, Hitachi S-4800) were applied for characterizing the microstructures of the materials, the corresponding element distribution was given by the energy spectrum analysis of high angle annular dark field scanning transmission electron microscope (HAADF-STEM), and the particle size distribution was measured by Nano particle

size analyzer and ZETA potential tester (Malvern Zetasizer Nano ZS90). Powder X-ray diffractometer (XRD, Rigaku Miniflex 600) equipped with a copper target was used to determine the crystal phase purity and the degree of crystallization. Variable temperature XRD (VT-XRD) measurement (Rigaku SmartLab) was used to identify the differences in thermal properties under N_2 atmosphere from ambient temperature to 700 °C with a heating rate of 10 °C/min. The sample was held at the target temperature for 5 min, and data were collected over the 2θ range of 5-50 ° with a step size of 20 °. Raman spectrum was collected by a Raman spectrometer (Labram, HR800) with a laser of 514.5 nm wavelength. The N_2 adsorption-desorption isotherms (77 K) and gas adsorption performance (298 K) were conducted on a physical adsorption instrument (Micromeritics ASAP2020). The specific surface area was calculated by the Brunauer-Emmett-Teller (BET) method, and the pore size distribution was calculated by the Density Functional Theory (DFT) model. The basicity of samples was measured by CO_2-temprature-programmed desorption (TPD, BELCAT-A). The surface element composition and valence state of the Pd@HCNs catalysts were analyzed by X-ray photoelectron spectrometer (XPS, ESCALAB 250) equipped with monochromatic Al Kα (1486.8 eV). The actual content of active components in the catalysts was measured by inductively coupled plasma optical emission spectrometer (ICP-OES, Optima 7000 DV). All microscope pictures were collected by an optical micro-scope (BX47, Olympus). The process was taken as movies by using an inverted microscope (Leica DMi8) equipped with a CCD camera (HAMAMATSU, C11440). Thermogravimetric analysis (TGA) was conducted on a TG analyzer (NETZSCH STA449 F3) under nitrogen atmosphere from ambient temperature to 900 °C with a heating rate of 10 °C/min.
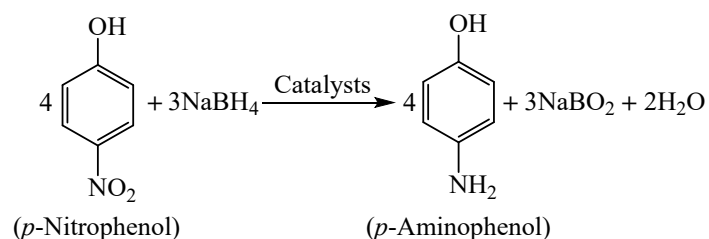
Evaluation of gas adsorption capacity

Adsorption isotherms of CO_2, CH_4, N_2 and H_2 were measured for HZIF-8 and SZIF-8. Approximately 100 mg of sample was weighed and loaded in to a sample holder. Each sample was first activated prior to the measurements. For this purpose, the sample was degassed under vacuum at 120 °C overnight. After activation, the sealed sample holder was connected to the analysis port. Adsorption isotherms of CO_2, CH_4, N_2 and H_2 gases were acquired up to 1.19 bar at 25 °C. Ideal selectivities of the samples were obtained by calculating the uptake values of different gases at the same pressure. The dynamic breakthrough curve of ZIF-8 was measured to analyze the separation performance of mixture gas. A quantity of ZIF-8 was filled into a fixed bed, which was heated for a pretreatment at 150 °C for 3 h. Then it was fed in a certain gas flow (CO_2/N_2, 15/85, v/v) of 10 mL/min at 20 °C and 0.1 MPa. The dynamic breakthrough curve was recorded by the auto gas chromatography. The gas volumes of crossing the empty bed and the sample bed are defined as C_0 and C_i, and the ratio of C_i and C_0 represents the volume of gas actually breaking through the sample bed.

Evaluation of catalytic performance

The hydrogenation of *p*-nitrophenol to *p*-aminophenol (Scheme 1) was used as a model reaction to evaluate the catalytic performance of Pd@HZIF-8 and Pd@SZIF-8. The typical reaction process was as follows: 0.1 g of *p*-nitrophenol was dissolved in the mixed solvent of water and ethanol (20 mL, $V_{water}:V_{ethanol} =1:1$) at 30 °C under agitation. 0.33 g of $NaBH_4$ was then added, followed by adding 0.1 g of catalyst to start the reaction. Samples were taken at fixed time intervals, and were analyzed by high-performance liquid chromatography (HPLC, Agilent 1200

Series, USA). After the reaction, the catalyst was separated by filtration, washed with a mixture of

water and ethanol, and then vacuum-dried for the next run.

$$4 \; \substack{\text{OH} \\ \text{(p-Nitrophenol)} \\ \text{NO}_2} + 3NaBH_4 \xrightarrow{\text{Catalysts}} 4 \; \substack{\text{OH} \\ \text{(p-Aminophenol)} \\ \text{NH}_2} + 3NaBO_2 + 2H_2O$$

Scheme S1. The catalytic hydrogenation of *p*-nitrophenol to *p*-aminophenol.

Liquid-phase phenol hydrogenation (Scheme 2) was used as a model reaction to evaluate the

catalytic performance of the obtained Pd@HCNs catalysts using a stainless-steel reactor (35 mL).

The reaction process was as follows: the catalyst (0.03 g) and phenol in cyclohexane (5 mL, 1

wt.%) were placed in the reactor in order. The reactor was sealed, and the atmosphere was

replaced with H_2 (0.2 MPa) five times. Then, the reactor was filled with 0.1 MPa H_2 and heated to

the desired temperature (80 °C) with stirring (100 rpm). After reaction for 30 min, the reactor was

cooled in a water bath.
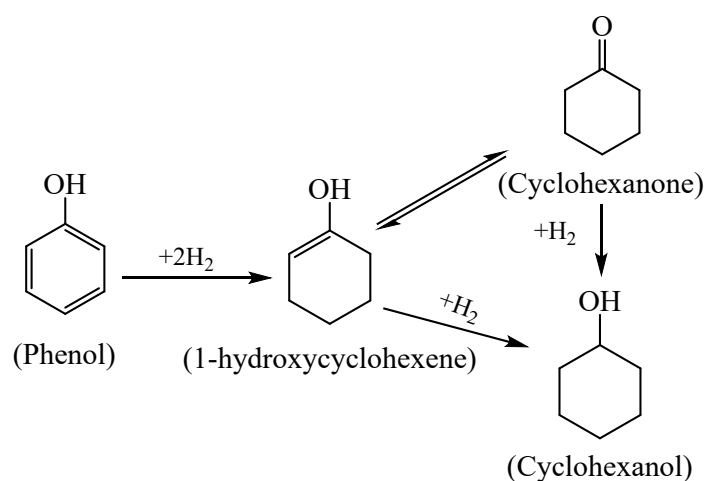
Scheme S2. Reaction pathways for phenol hydrogenation.

Finally, a clear liquid was obtained from the reactor by filtration, and quantitative analysis

was carried out via gas chromatography (Shimadzu GC 2014). The products were identified by

nuclear magnetic resonance (NMR, obtained on a JNM-ECZ400S spectrometer with CDCl$_3$ as a solvent, 400 MHz). The concentrations of phenol and cyclohexanone in the reaction mixture were obtained according to the GC results using the internal standard method (trimethylbenzene was used as an internal standard). The phenol conversion and cyclohexanone selectivity were calculated by the following equations:

$$\text{Conversion (\%)} = \frac{\text{(Initial moles of phenol)} - \text{(Final moles of phenol)}}{\text{Initial moles of phenol}} \times 100\%$$

$$\text{Selectivity (\%)} = \frac{\text{Moles of cyclohexanone}}{\text{(Initial moles of phenol)} - \text{(Final moles of phenol)}} \times 100\%$$

The hydrogenation of nitroarenes and phenols with different functional groups with the as-developed catalysts were carried out.
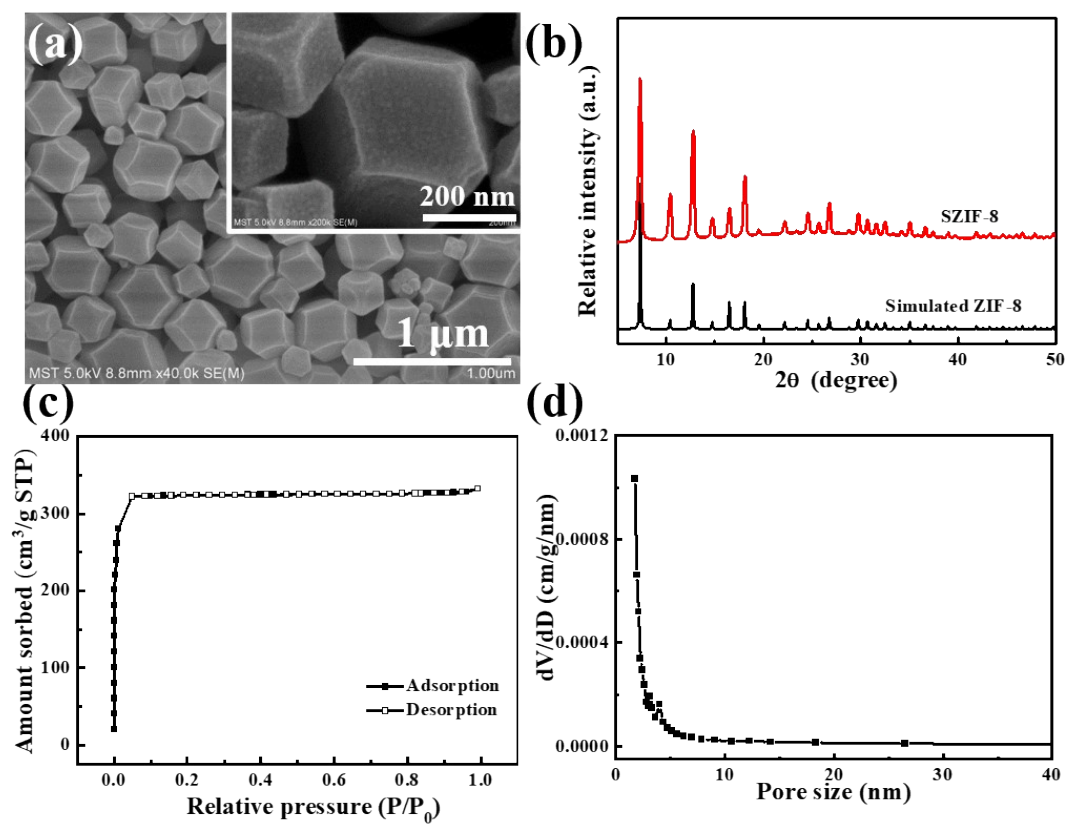
Fig. S1 FESEM image (a), XRD patterns (b), N$_2$ sorption isotherms (c) and BJH pore size

distribution curve (d) of SZIF-8.
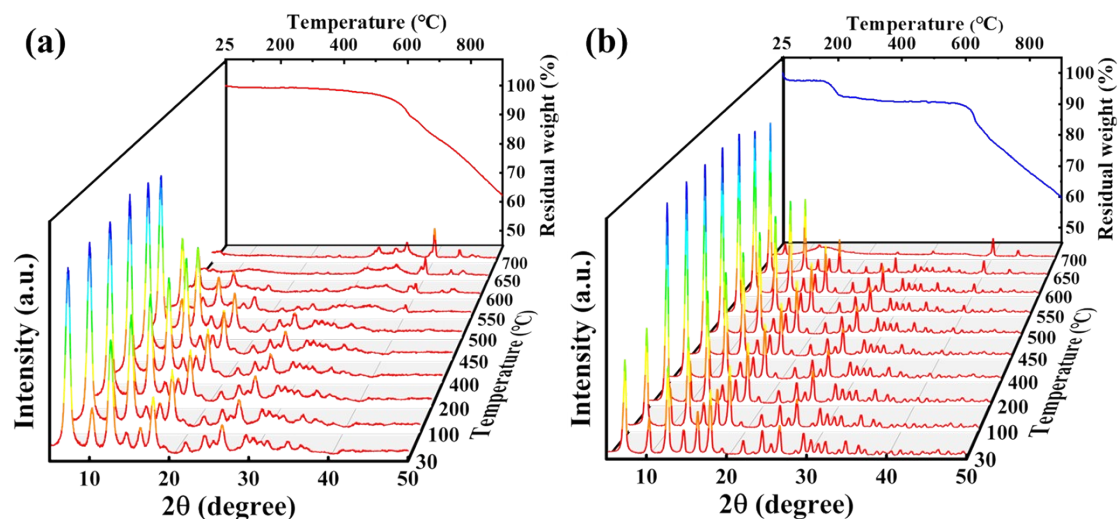
Fig. S2 TG curves and VT-XRD patterns of HZIF-8 (a) and SZIF-8 (b).

The TG curves and VT-XRD patterns of HZIF-8 and SZIF-8 are shown in Fig. S2. For HZIF-8, the characteristic peaks belonging to ZIF-8 in the VT-XRD patterns start to weaken after 500 °C, indicating a phase transition in the sample, which is consistent with the weight loss curve (Fig. S2a). In the TG curve of SZIF-8, the weight loss before 200 °C comes from the volatilization of free or poorly bound water and imidazole in the sample,[1] and the gradual weight loss after 600 °C is induced by the thermal decomposition of the material, almost in line with the VT-XRD patterns (Fig. S2b). The results in Fig. S2 reveal the slightly low thermal stability of HZIF-8 as compared to SZIF-8.[2]
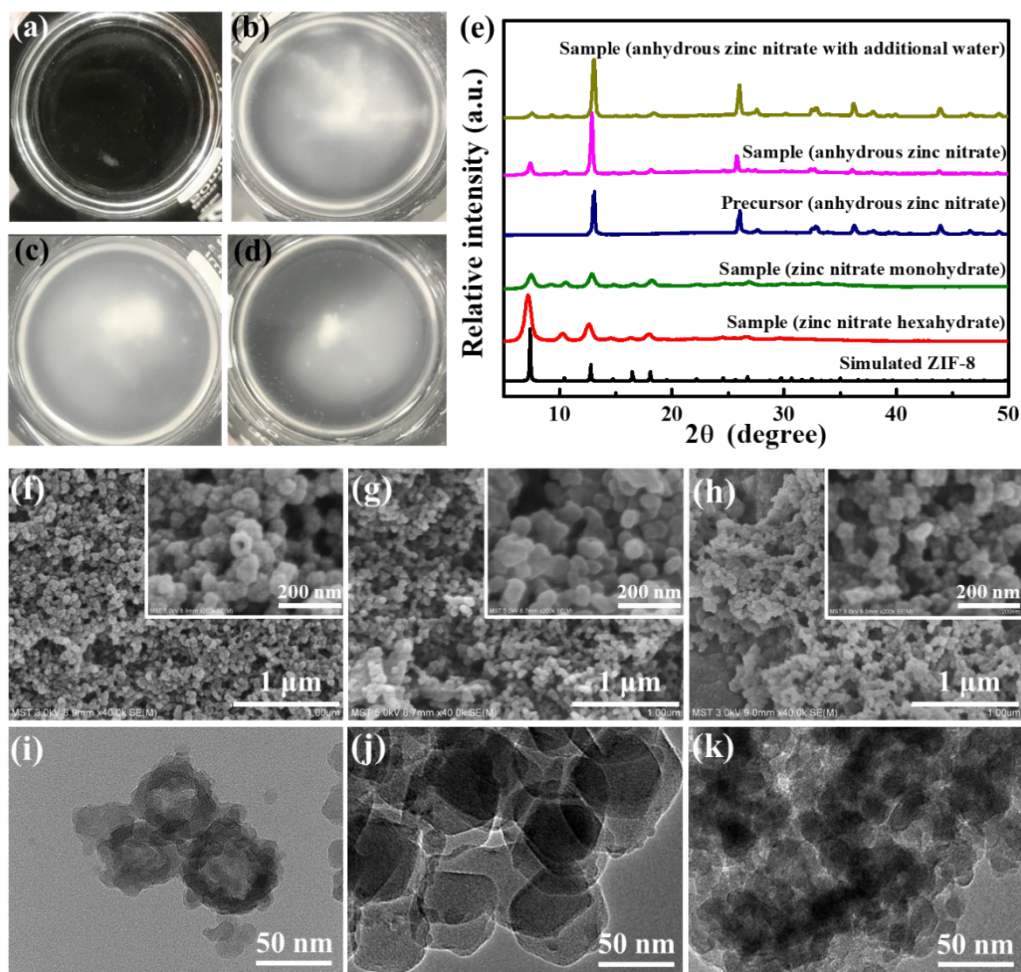
Fig. S3 Photographs of the zinc nitrate with different contents of hydration water in 1-octanol: zinc nitrate hexahydrate (blank control) (a), zinc nitrate monohydrate (b), anhydrous zinc nitrate (c), and anhydrous zinc nitrate with additional water (d); XRD patterns of samples prepared with zinc nitrate with different hydration water contents (e); FESEM images (f-h) and TEM images (i-k) of samples prepared with zinc nitrate with different hydration water contents as the precursors: zinc nitrate monohydrate (f, i), anhydrous zinc nitrate (g, j), and anhydrous zinc nitrate with additional water (h, k).
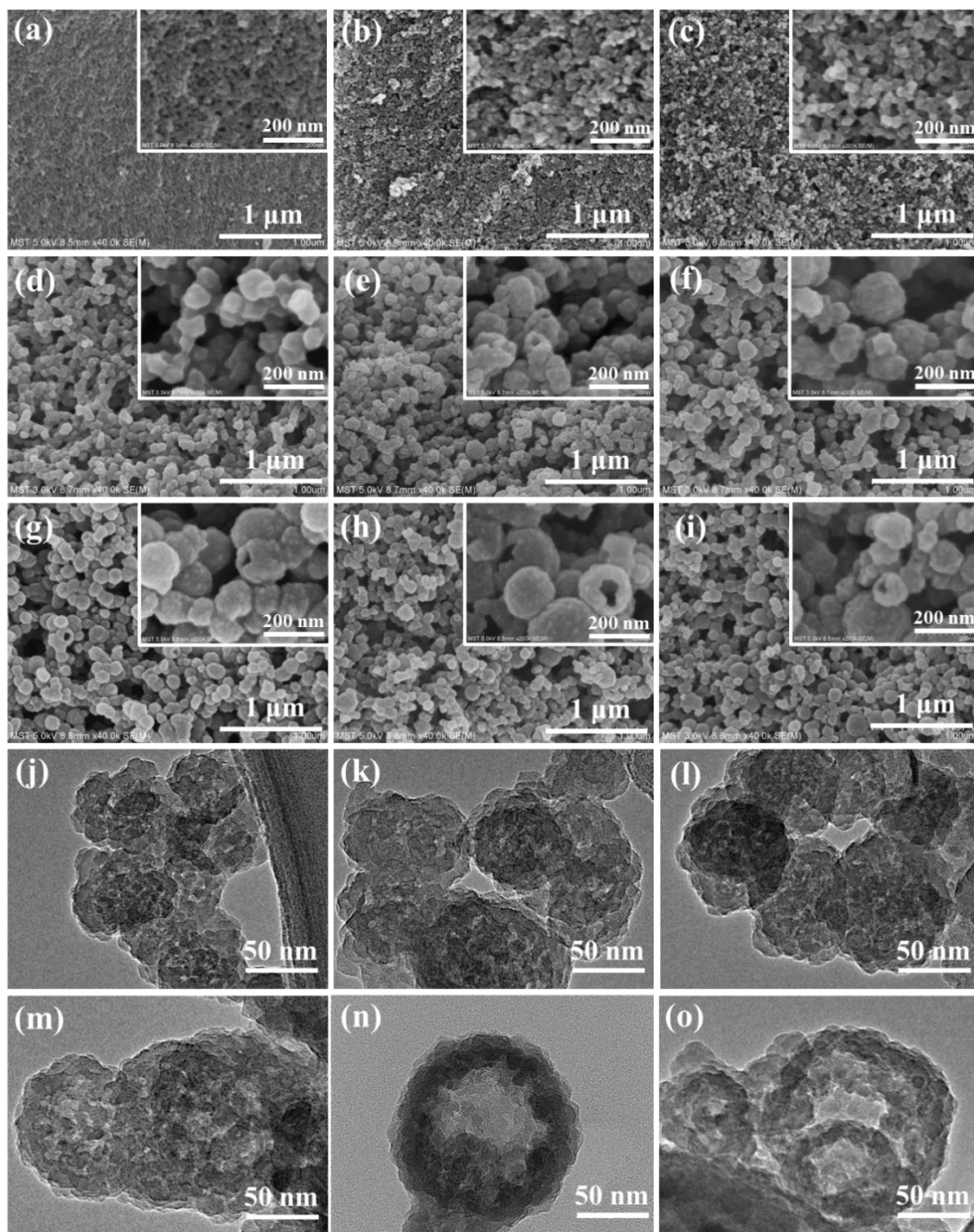
Fig. S4 FESEM images (a-i) and TEM images (j-o) of ZIF-8 samples obtained in different solvents: methanol (a), ethanol (b), 1-propanol (c), 1-butanol (d, j), 1-pentanol (e, k), 1-hexanol (f, l), 1-heptanol (g, m), 1-nonanol (h, n), and 1-decanol (i, o).
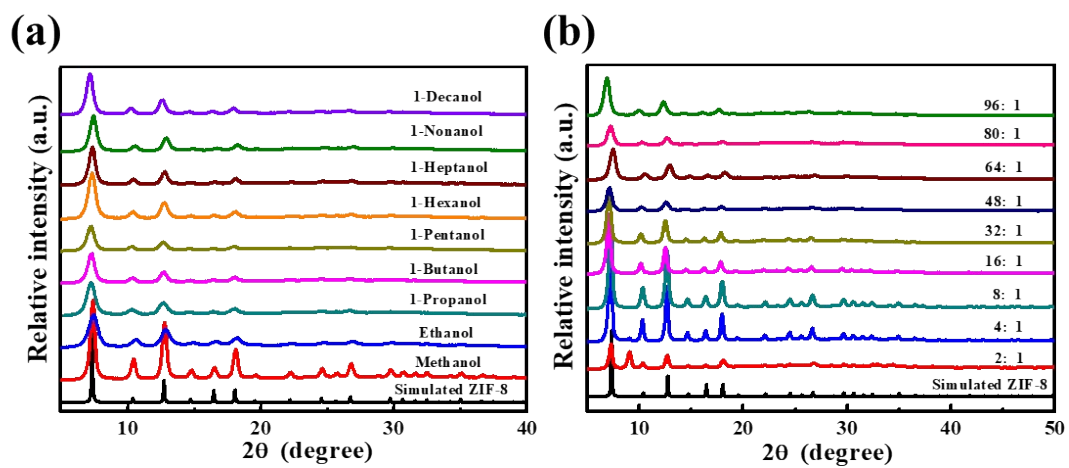
Fig. S5 XRD patterns of ZIF-8 samples obtained in different solvents (a) and prepared with different 2-MeIM/Zn^{2+} molar ratios (b).
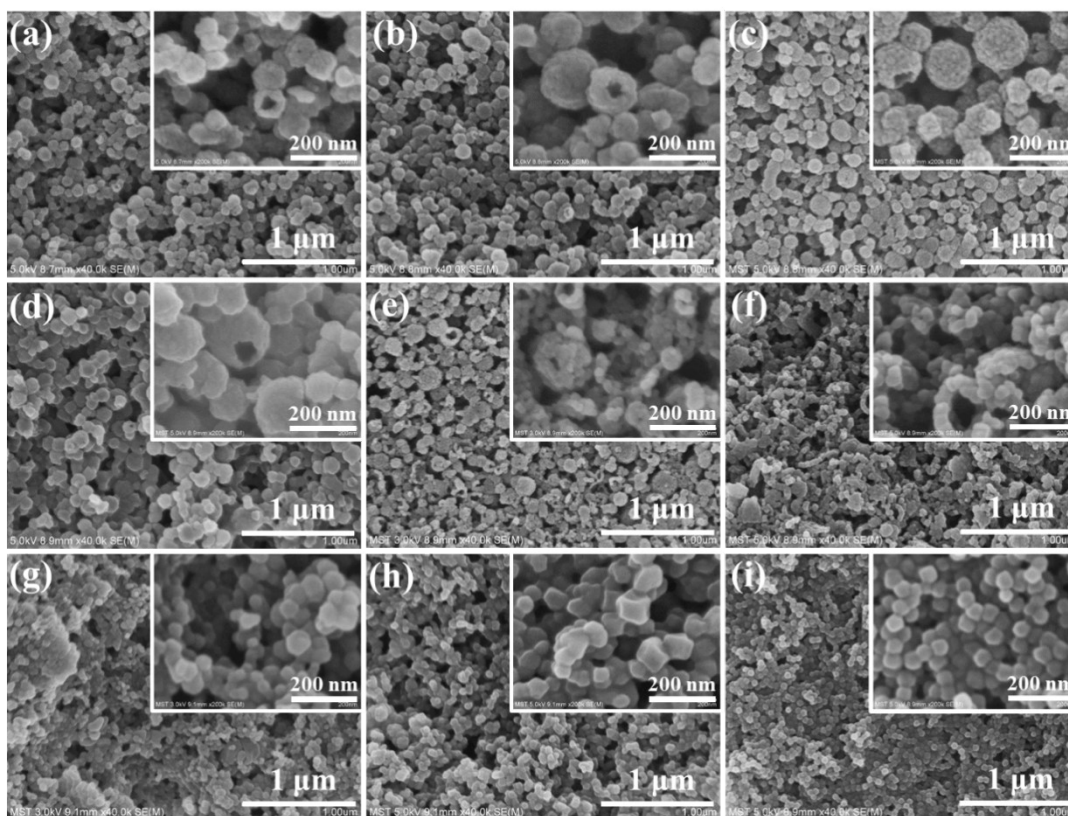
Fig. S6 FESEM images of ZIF-8 samples prepared with different 2-MeIM/Zn^{2+} molar ratios: 96:

1 (a), 80: 1 (b), 64: 1(c), 48: 1 (d), 32: 1 (e), 16: 1 (f), 8: 1 (g), 4: 1 (h), and 2: 1 (i).

In this work, the change of 2-MeIM/Zn^{2+}ratio is realized by changing the concentration of

zinc nitrate·hexahydrate with fixed 2-MeIM concentration.
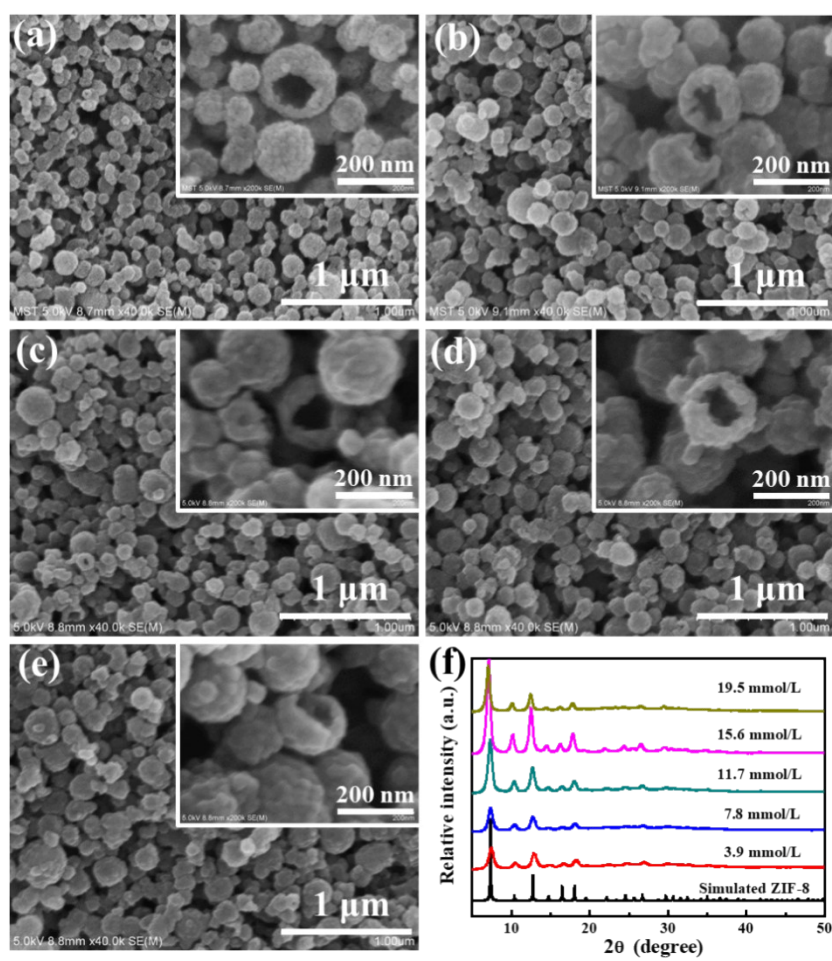
Fig. S7 FESEM images of HZIF-8 obtained with different concentrations of Zn^{2+} (the molar ratio

of 2-MeIM/Zn^{2+} is 64: 1): 3.9 (a), 7.8 (b), 11.7 (c), 15.6 (d), and 19.5 mol/L (e); The

corresponding XRD patterns (f).
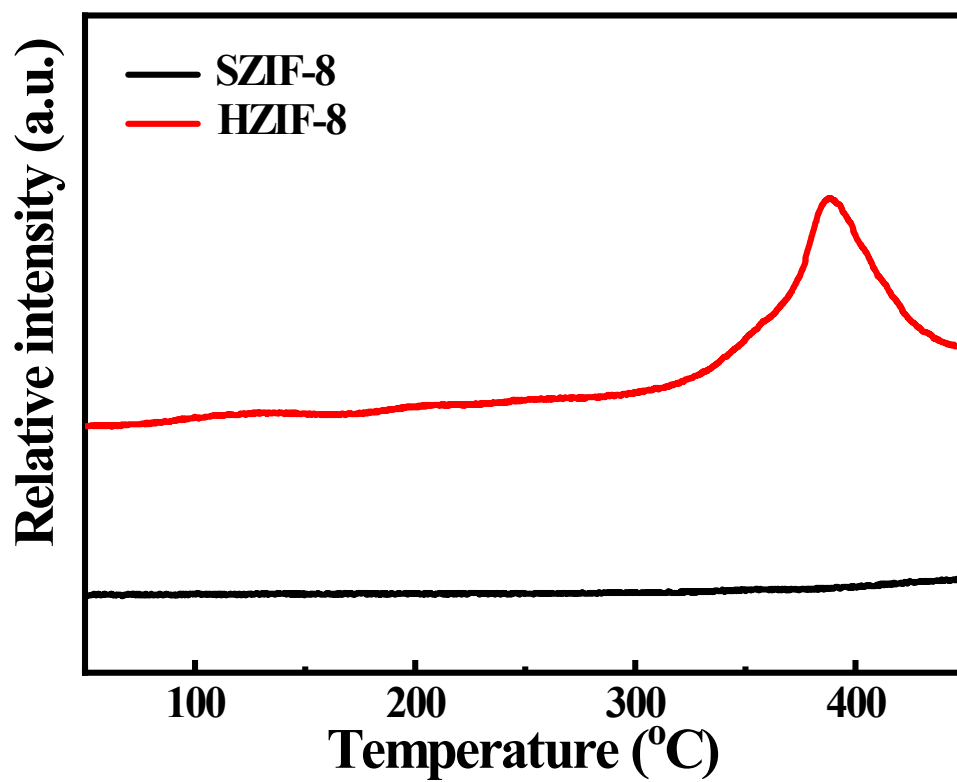
Fig. S8 CO$_2$-TPD patterns of HZIF-8 and SZIF-8.
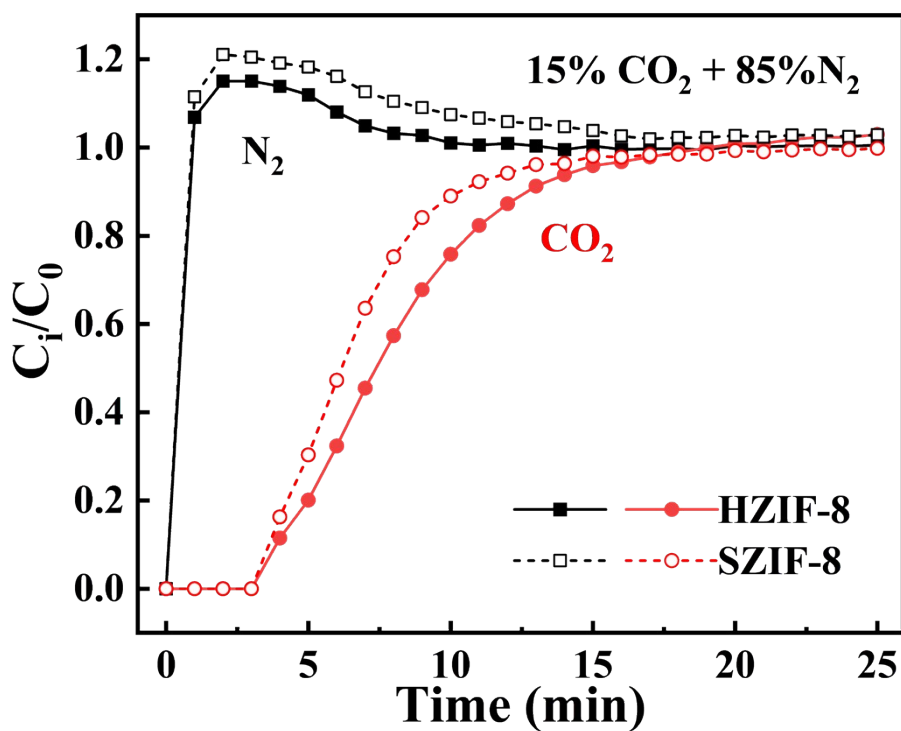
Fig. S9 Dynamic breakthrough curves of CO_2/N_2 over HZIF-8 and SZIF-8.

As displayed in Fig. S9, N_2 is the first component to break through the fixed bed, indicating that N_2 is hardly adsorbed by ZIF-8. Interestingly, the breakthrough amount of CO_2 over HZIF-8 is less than that over SZIF-8, which indicates that HZIF-8 possesses good selective adsorption performance for CO_2 as compared to SZIF-8. The results match well with the pure CO_2 and N_2 uptakes (Fig. 3a).
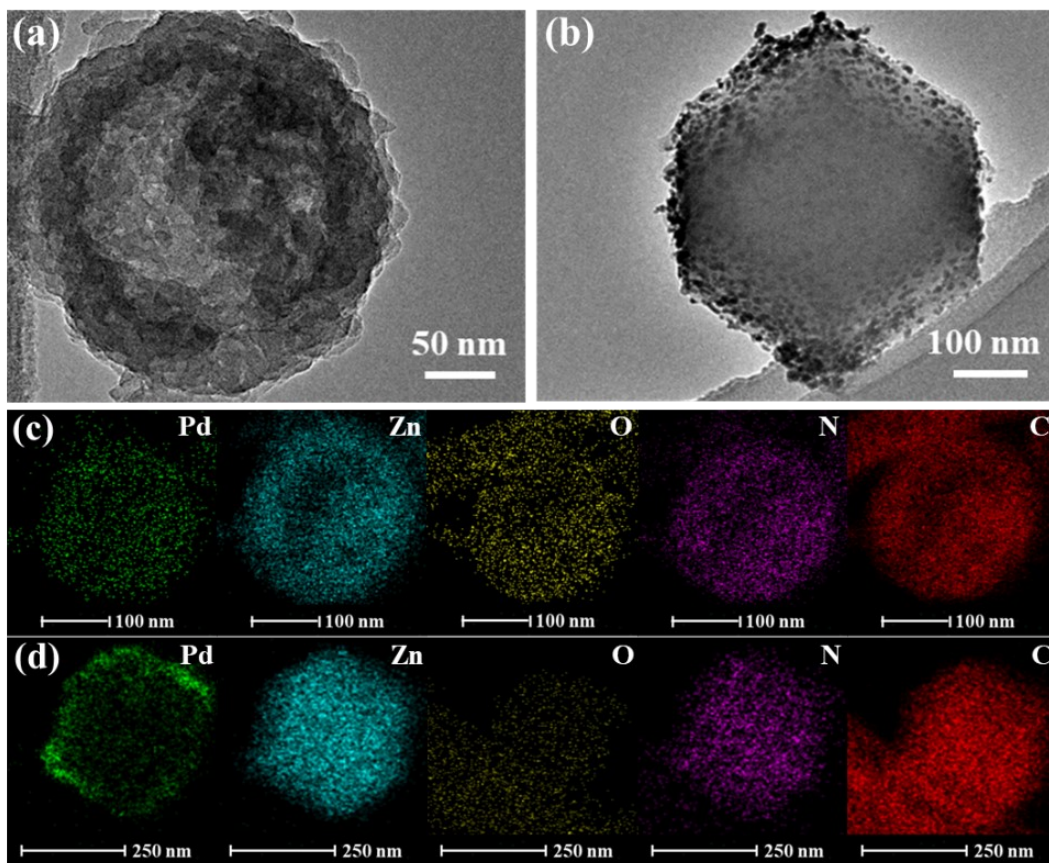
Fig. S10 TEM images and elemental mapping images of Pd@HZIF-8 (a, c) and Pd@SZIF-8 (b, d).
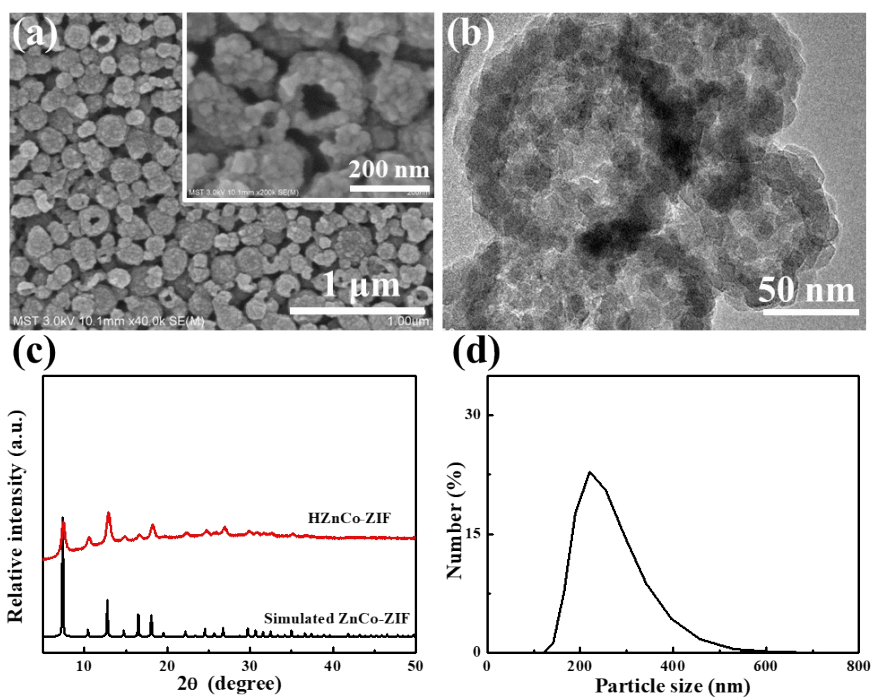
**Fig. S11** FESEM image (a), TEM image (b), XRD patterns (c) and particle size distribution (d) of

HZIF-Zn/Co.
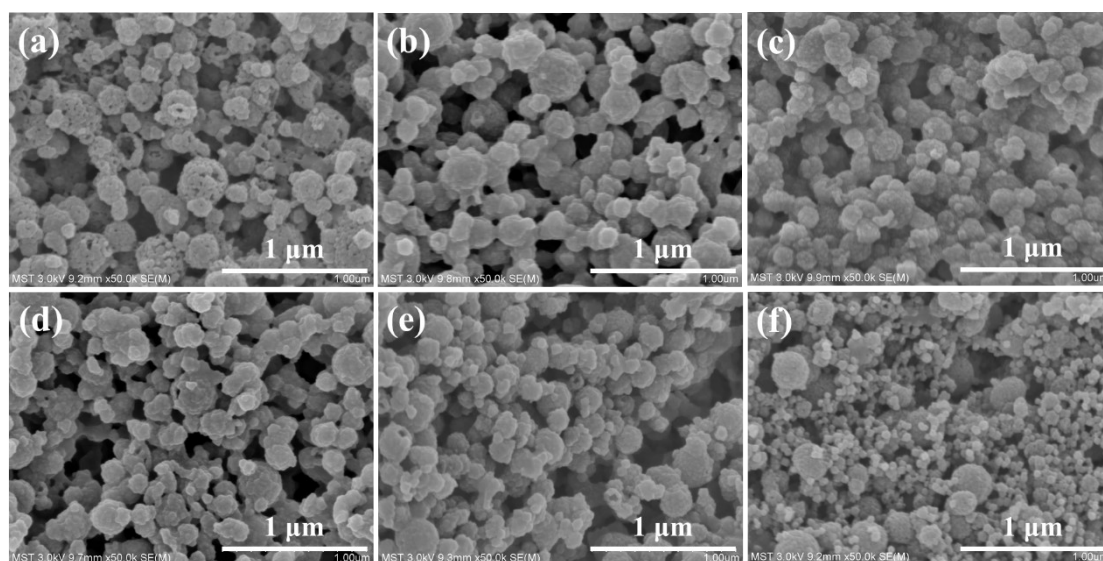
Fig. S12 FESEM images of HZIF-0.6-6 (a), HZIF-0.9-6 (b), HZIF-1.2-6 (c), HZIF-1.5-6 (d),

HZIF-2.4-6 (e), and HZIF-3.6-6 (f).

At fixed concentration of $Co(NO_3)_2 \cdot 6H_2O$ and hydration number, the droplet size is consistent. When using low concentration of imidazole, due to the short nucleation time and long growth time of ZIF-67 granules, a few of ZIF-67 granules with large particle size are formed,[3] which are not enough to form a complete HZIF-x-y sphere without holes (Fig. S12a). When the concentration of imidazole reaches 3.6 mol/L, a large number of scattered ZIF-67 granules appear in the sample, which may be induced by the fast nucleation (Fig. S12f).[4]
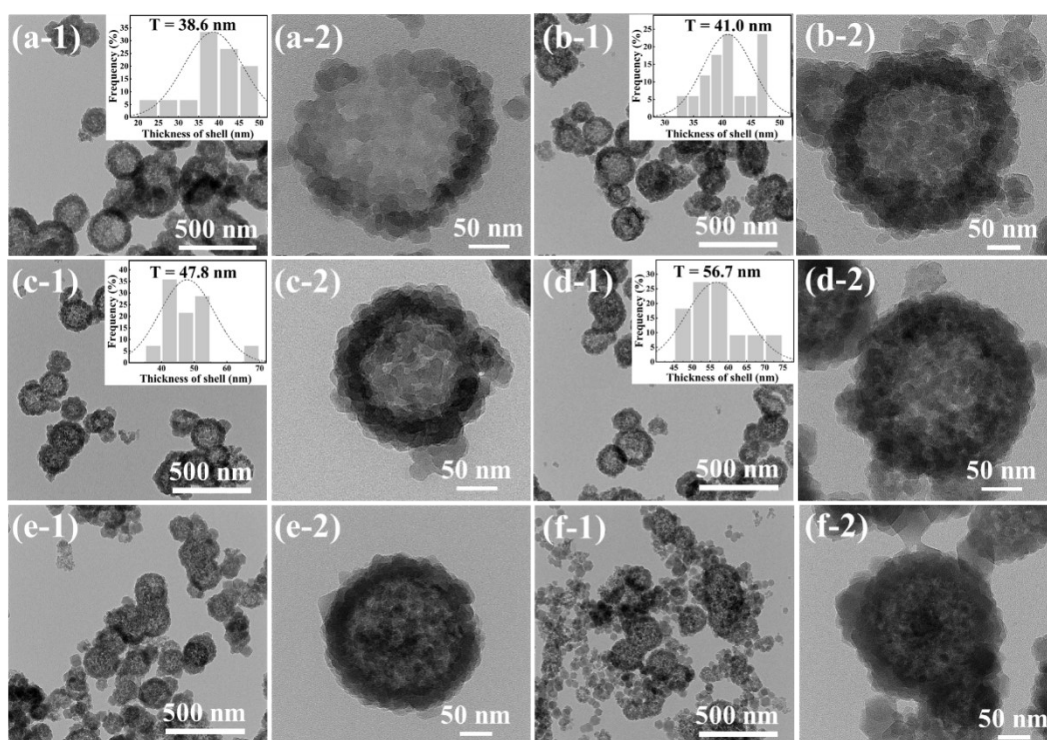
Fig. S13 TEM images of HZIF-0.6-6 (a-1, a-2), HZIF-0.9-6 (b-1, b-2), HZIF-1.2-6 (c-1, c-2), HZIF-1.5-6 (d-1, d-2), HZIF-2.4-6 (e-1, e-2), and HZIF-3.6-6 (f-1, f-2). The inset is the shell thickness of corresponding HZIFs.

When the concentration of imidazole increases, the morphology changes from large intact and broken spherical particles with holes on the surface to smaller intact spherical particles, and then to a mixture of a large number of scattered irregular particles and a few of spherical particles (Figs. S12 and S13).

The shell thickness rises with increasing imidazole concentration (Fig. S13), because high imidazole concentration causes more ligand molecules to diffuse more quickly into the droplets to react with Co^{2+}.
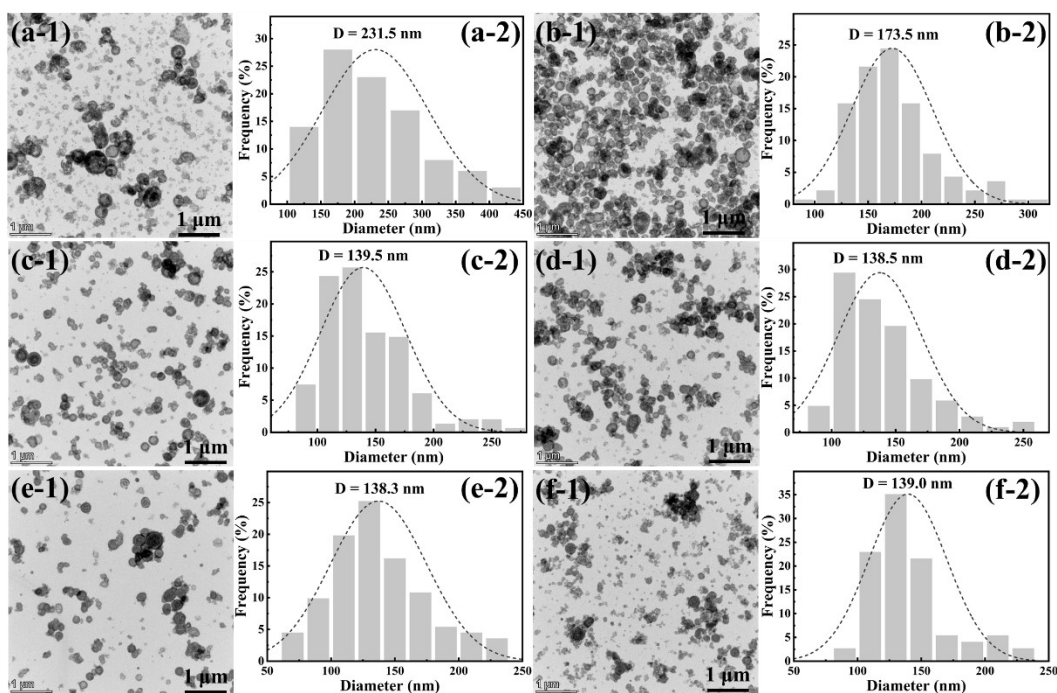
Fig. S14 TEM images of HZIF-0.6-6 (a-1), HZIF-0.9-6 (b-1), HZIF-1.2-6 (c-1), HZIF-1.5-6 (d-1), HZIF-2.4-6 (e-1), and HZIF-3.6-6 (f-1); diameter distribution of HZIF-0.6-6 (a-2), HZIF-0.9-6 (b-2), HZIF-1.2-6 (c-2), HZIF-1.5-6 (d-2), HZIF-2.4-6 (e-2), and HZIF-3.6-6 (f-2).

When the concentration of imidazole increases, the particle size of ZIF-67 granules becomes smaller and the particle size of HZIF-x-y also decreases. With the further increase in the imidazole concentration, the particle size of ZIF-67 granules basically remains unchanged due to limited metal ions in 1-octanol, and as a result, the size of HZIF-x-y also remains unchanged (Fig. S14).
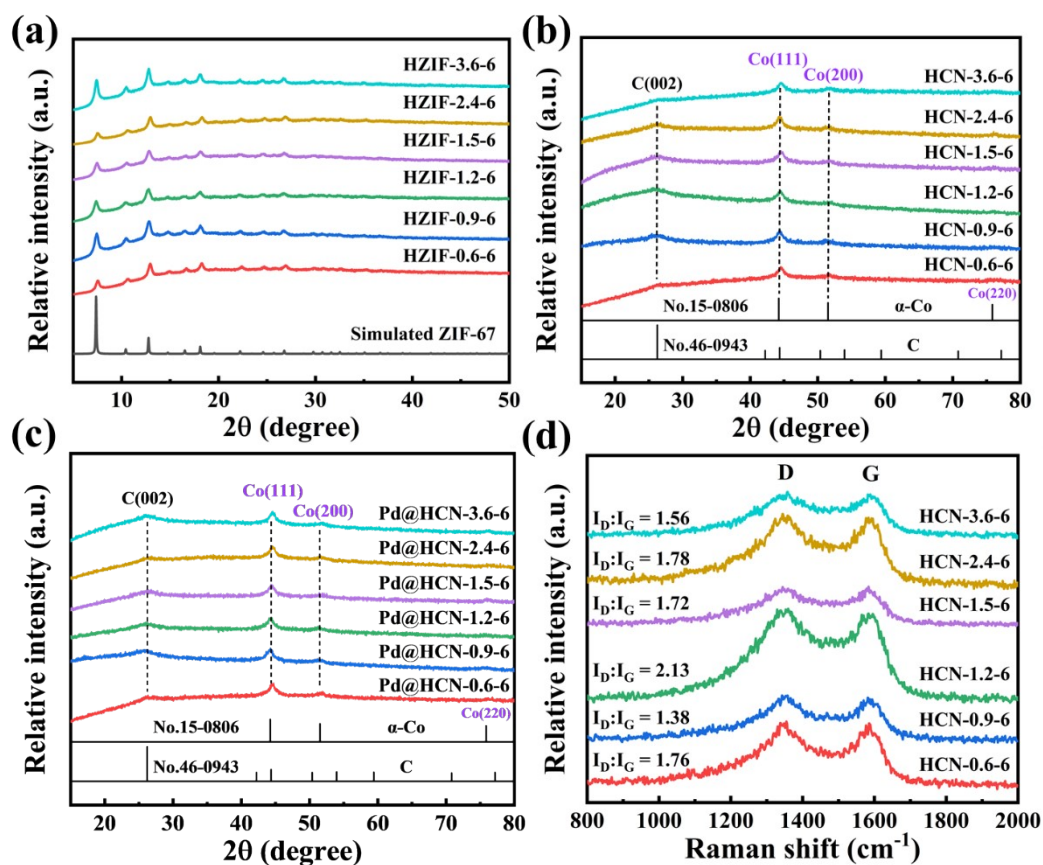
Fig. S15 XRD patterns of HZIFs (a), HCNs (b), and Pd@HCNs (c); Raman spectra of HCNs (d).
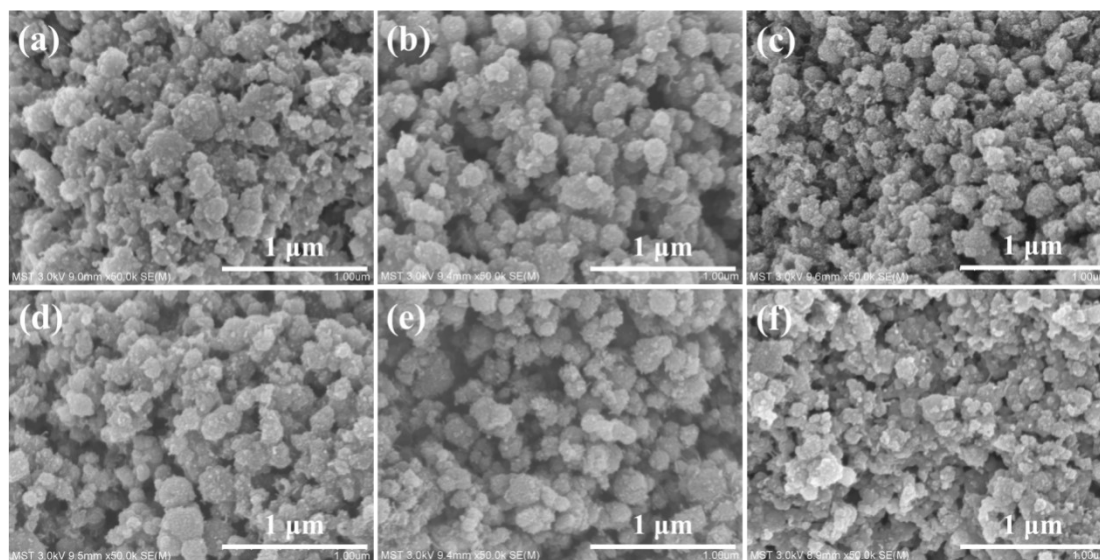
Fig. S16 FESEM images of HCN-0.6-6 (a), HCN-0.9-6 (b), HCN-1.2-6 (c), HCN-1.5-6 (d),

HCN-2.4-6 (e), and HCN-3.6-6 (f).
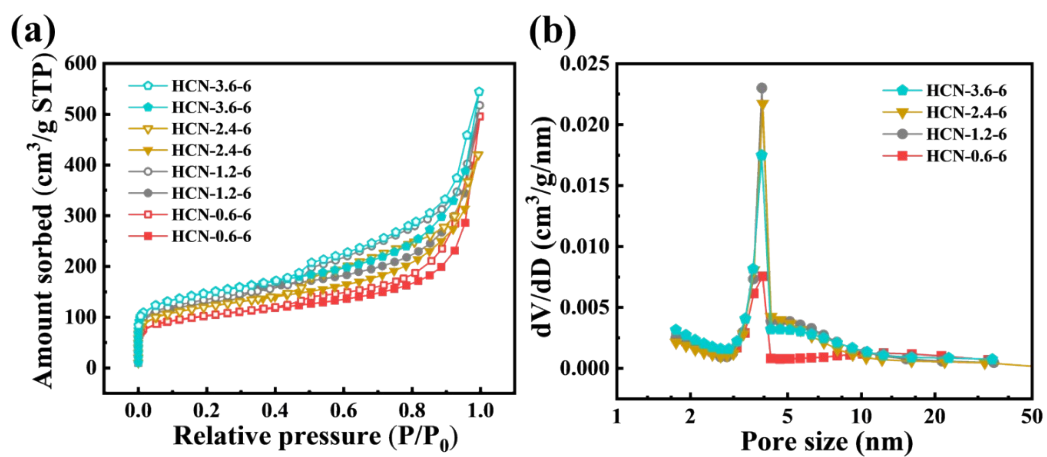
Fig. S17 N_2 sorption isotherms (a) and mesopore size distribution curves (b) of HCNs.
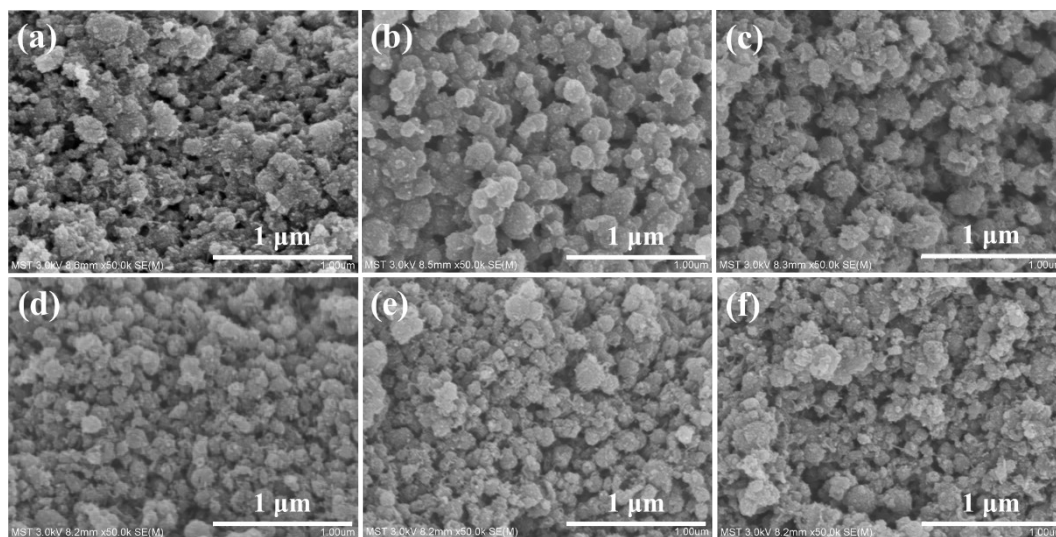
Fig. S18 FESEM images of Pd@HCN-0.6-6 (a), Pd@HCN-0.9-6 (b), Pd@HCN-1.2-6 (c),
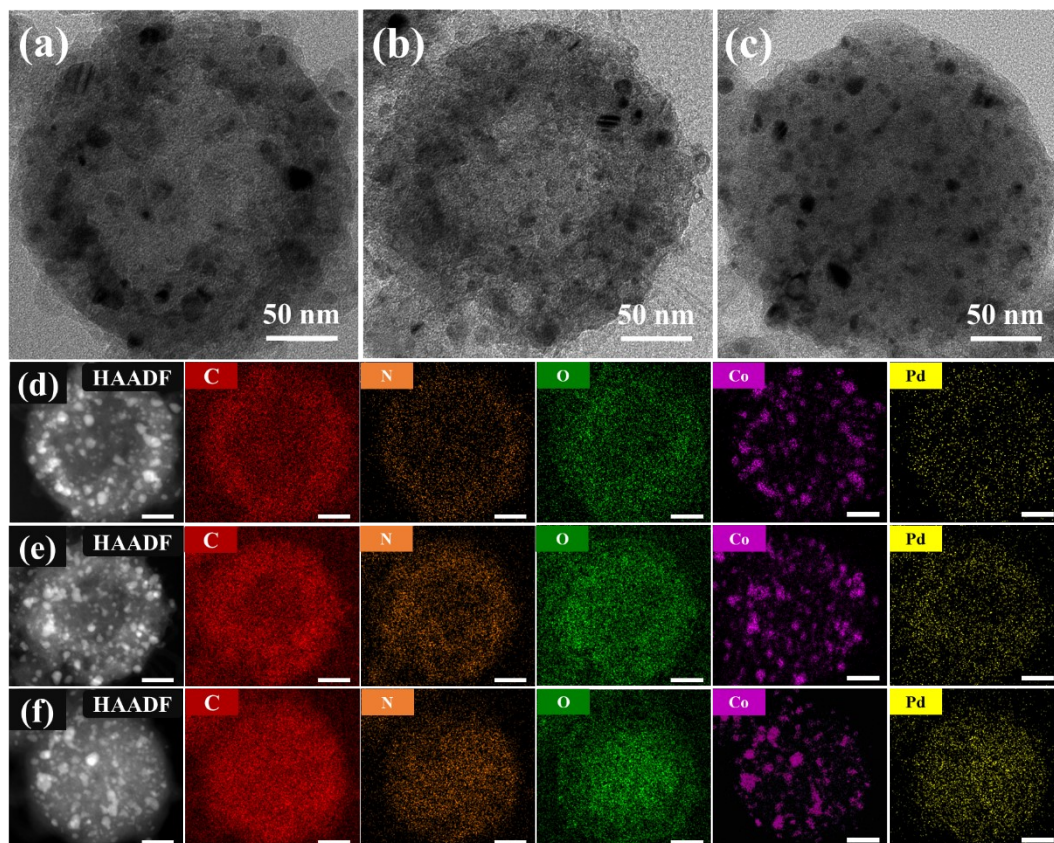
Pd@HCN-1.5-6 (d), Pd@HCN-2.4-6 (e), and Pd@HCN-3.6-6 (f).

Fig. 19 TEM images of Pd@HCN-0.6-6 (a), Pd@HCN-1.2-6 (b), and Pd@HCN-2.4-6 (c);

HAADF and elemental mapping images of Pd@HCN-0.6-6 (d), Pd@HCN-1.2-6 (e), and

Pd@HCN-2.4-6 (f). Scale bars in the images: 50 nm.
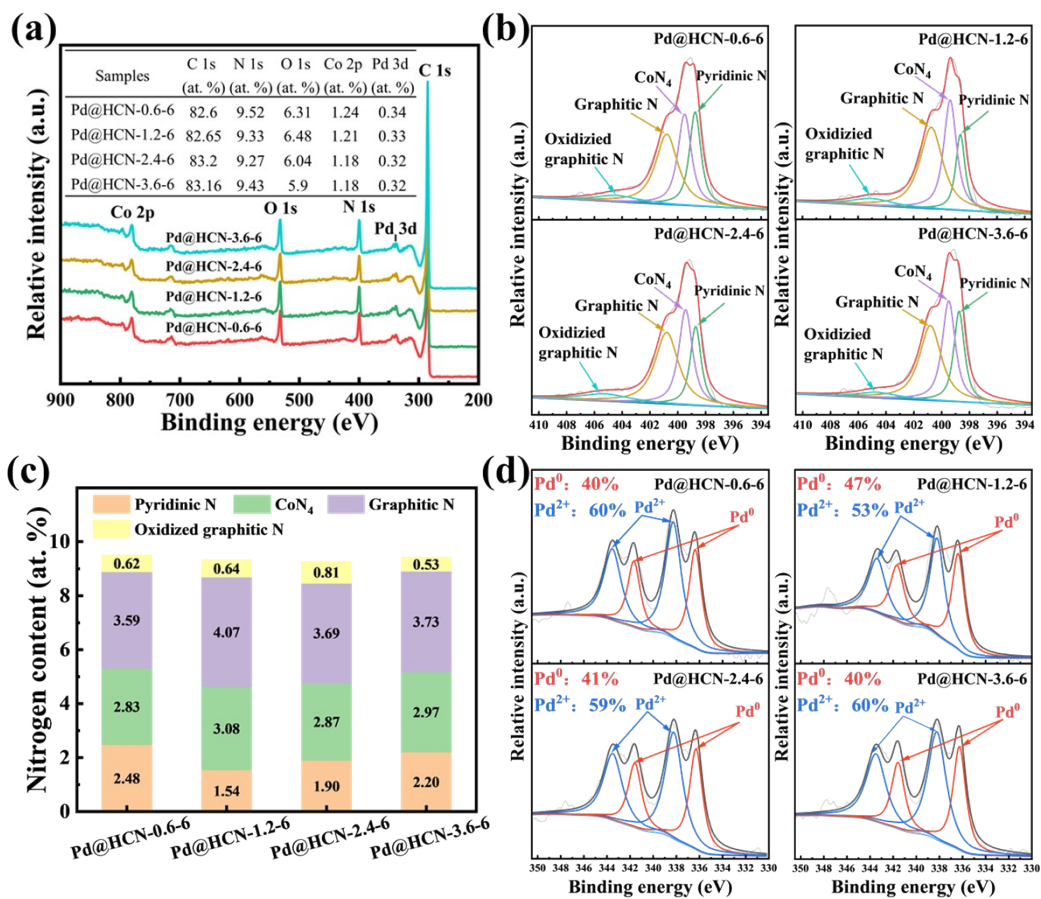
Fig. S20 XPS results and survey spectra (a), N 1s spectra (b), N-species content (c), and Pd 3d spectra (d) in Pd@HCNs catalysts.
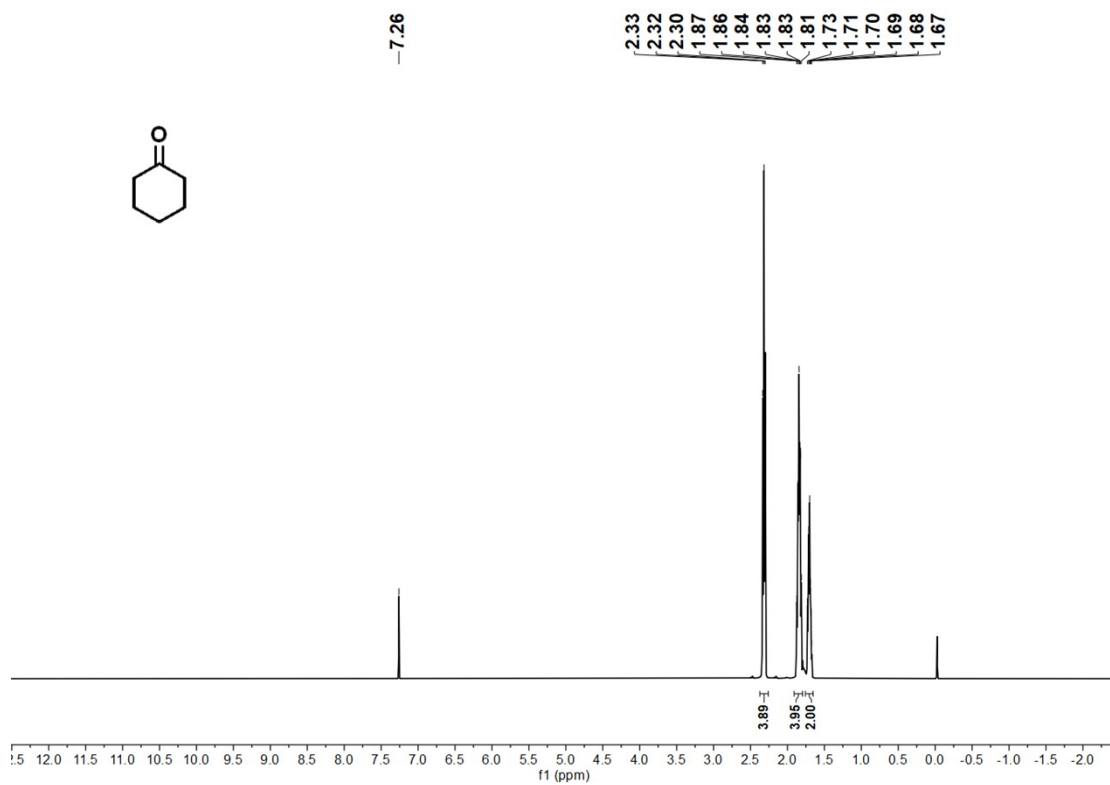
Fig. S21 ^{1}H-NMR of the major product.
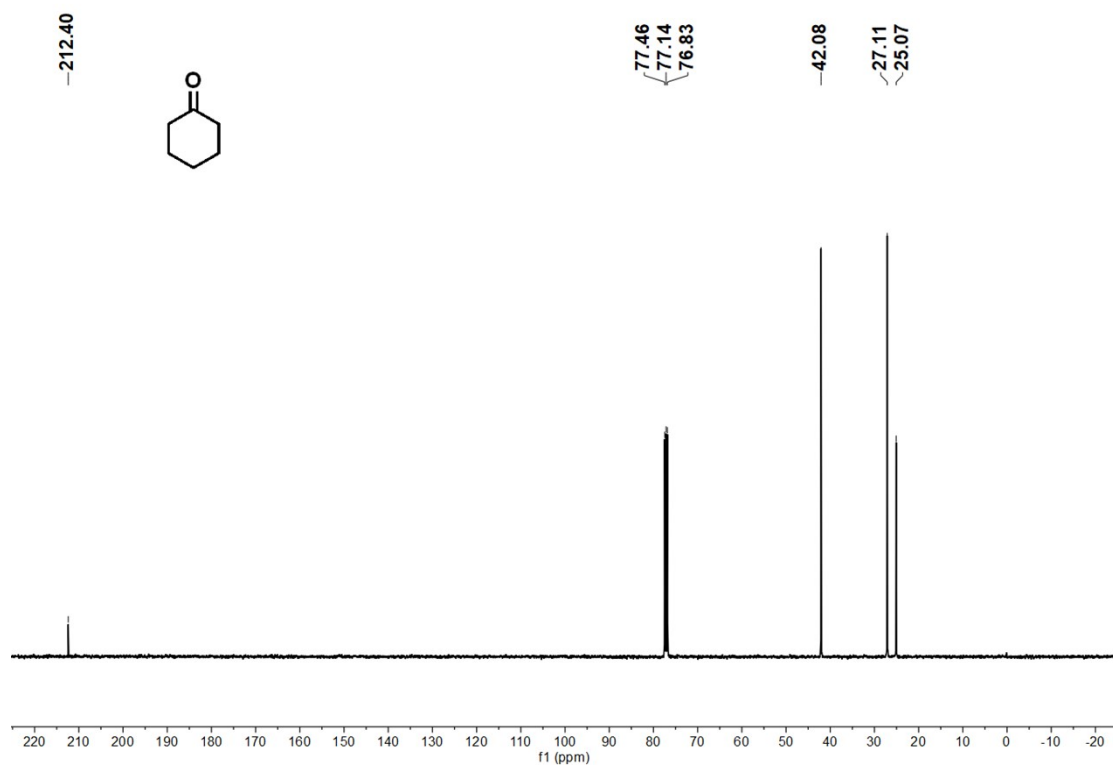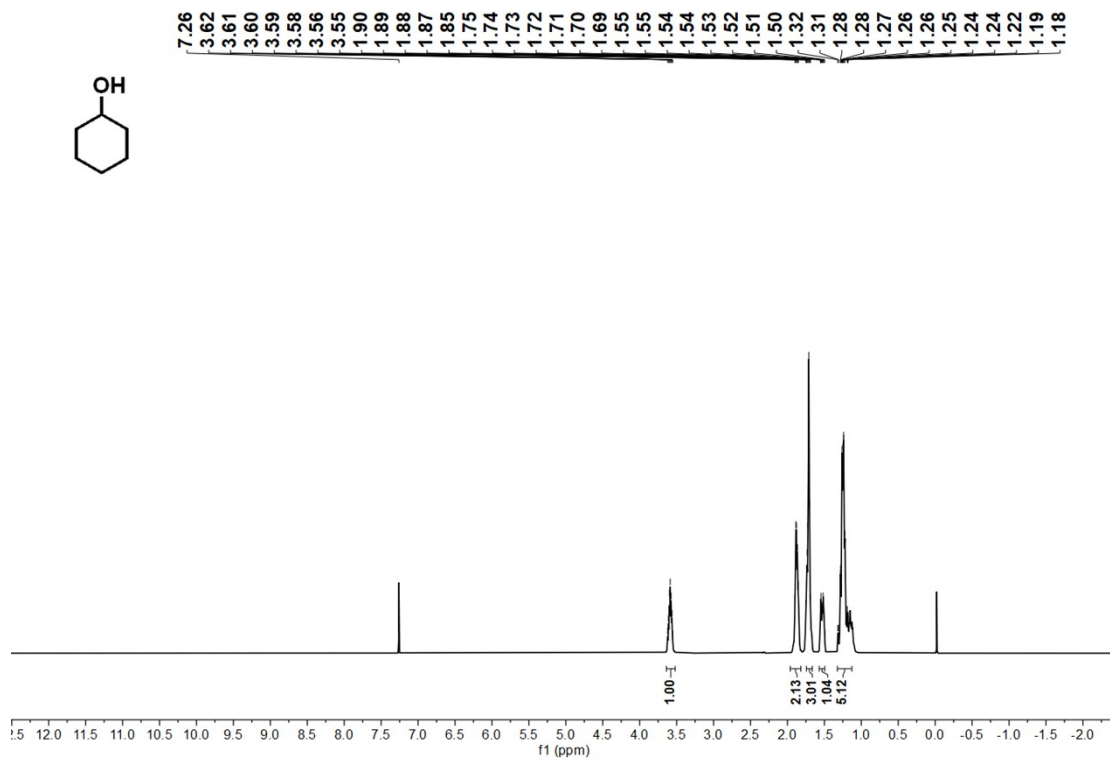
Fig. S22 ^{13}C-NMR of the major product.

Fig. S23 ^{1}H-NMR of the by-product.

OH

77.46
77.14
76.82
70.42
36.09
25.52
24.24

220 210 200 190 180 170 160 150 140 130 120 110 100 90 80 70 60 50 40 30 20 10 0 -10 -20
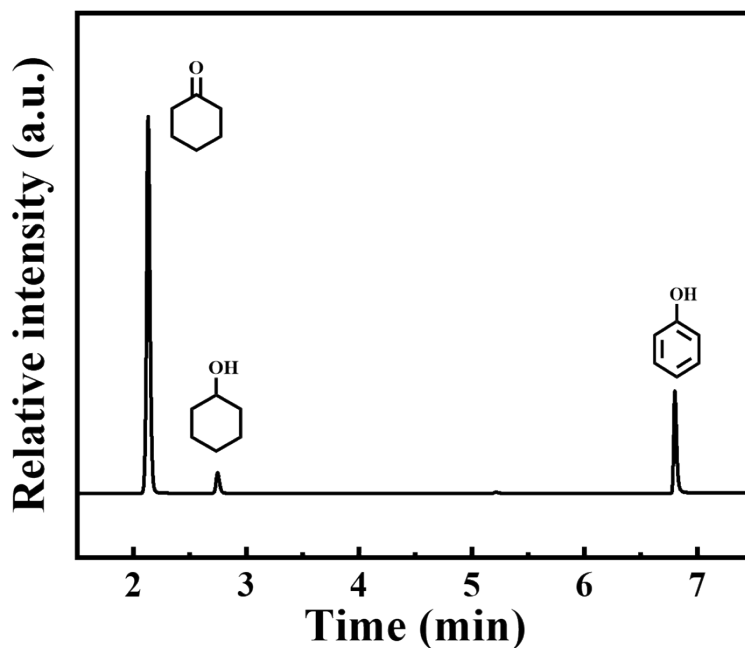f1 (ppm)
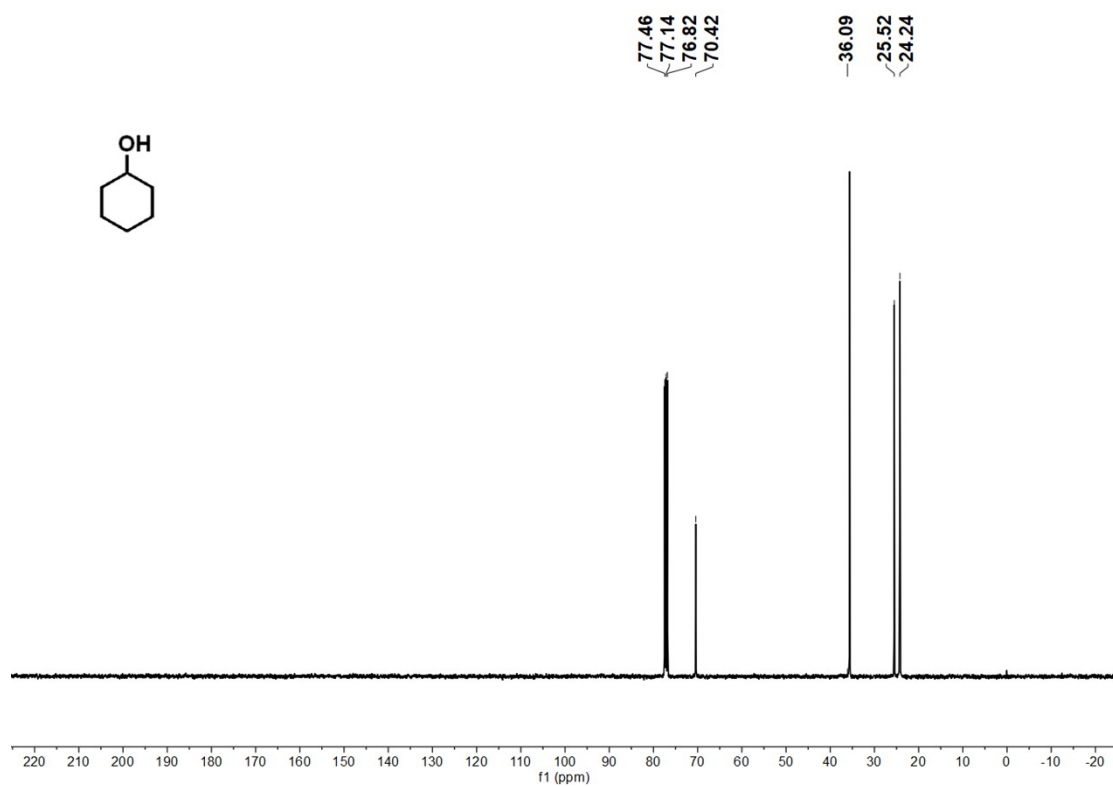
Fig. S24 ^{13}C-NMR of the by-product.

Fig. S25 Typical GC analysis of the reaction mixture of phenol hydrogenation.

According to the NMR results (Figs. S21 and S22), ^{1}H-NMR (400 MHz, CDCl$_3$) δ = 2.33-2.30 (m, 4 H), 1.87-1.81 (m, 4 H), 1.73-1.67 (m, 2 H) and ^{13}C-NMR (400 MHz, CDCl$_3$) δ = 212.40 (1C), 42.08 (2C), 27.11 (2C), 25.07 (1C), we can confirm that the major product of selective phenol hydrogenation is cyclohexanone. According to the NMR results (Figs. S23 and S24), ^{1}H-NMR (400 MHz, CDCl$_3$) δ = 3.62-3.55 (m, 1 H), 1.90-1.85 (m, 2 H), 1.75-1.69 (m, 3 H) 1.55-1.50 (m, 1 H) 1.32-1.18 (m, 5 H) and ^{13}C-NMR (400 MHz, CDCl$_3$) δ = 70.42 (1C), 36.09 (2C), 25.52 (2C), 24.24 (1C), we can confirm that the by-product of selective phenol hydrogenation is cyclohexanol. The concentrations of phenol and cyclohexanone in the reaction mixture were obtained according to the GC results (Fig. S25), and then the phenol conversion and cyclohexanone selectivity were calculated.
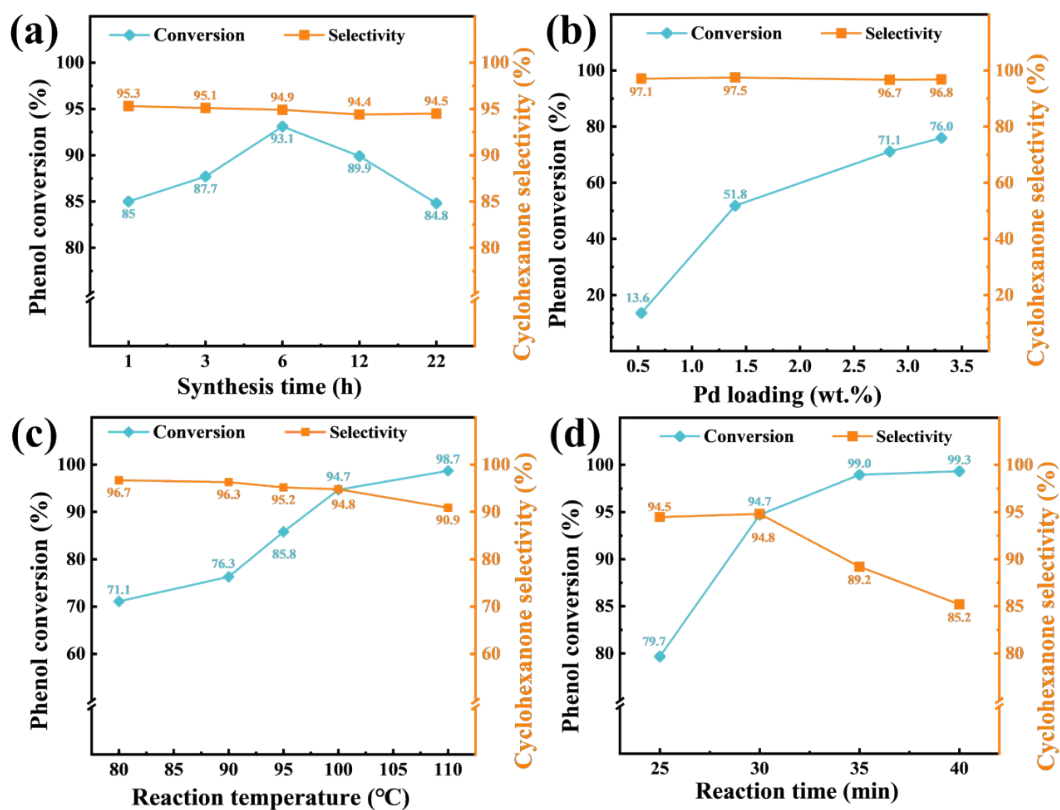
S33

Fig. S26 Catalytic performance of Pd@HCNs catalysts: the effect of HZIFs synthesis time (catalyst synthesis conditions: theoretical Pd loading 2 wt.%; reaction conditions: 1 wt.% phenol cyclohexane solution 5 mL, catalyst 0.03 g, 0.1 MPa H_2, 80 ^{o}C, 60 min) (a); the effect of Pd loading (catalyst synthesis conditions: 6 h; reaction conditions: 1 wt.% phenol cyclohexane solution 5 mL, catalyst 0.03 g, 0.1 MPa H_2, 80 ^{o}C, 60 min) (b); the effect of reaction temperature (catalyst synthesis conditions: Pd loading 2.8 wt.%, 6 h; reaction conditions: 1 wt.% phenol cyclohexane solution 5 mL, catalyst 0.03 g, 0.1 MPa H_2, 80 ^{o}C, 30 min) (c); the effect of reaction time (catalyst synthesis conditions: Pd loading 2.8 wt.%, 6 h; reaction conditions: 1 wt.% phenol cyclohexane solution 5 mL, catalyst 0.03 g, 0.1 MPa H_2, 100 ^{o}C) (d).

Fig. S27 Magnetic collection of Pd@HCN-1.2-6 by a magnet.

Table S1 Porous properties of HZIF-8 and SZIF-8

Samples	S_{BET} (m^2/g)	S_{meso}/S_{BET} (%)	V_{pore} (cm^3/g)	V_{meso}/V_{pore} (%)
HZIF-8	1365	20.3	1.02	57.2
SZIF-8	1376	1.1	0.51	3.9

Table S2 Comparison of CO_2, CH_4, N_2 and H_2 adsorption capacities of ZIF-8 synthesized in this

study and reported in literature

Samples	Gas adsorption capacity (mmol/g)[a]				References
	CO_2	CH_4	N_2	H_2	
HZIF-8	1.37	0.48	0.11	0.09	This work
SZIF-8	0.63	0.27	0.10	0.08	This work
ZIF-8	0.66	0.24			[5]
ZIF-8	0.65	0.25	0.05	0.007	[6]
ZIF-8	0.67	0.25	0.09		[7]
ZIF-8	0.89		0.11		[8]
ZIF-8	0.50	0.25	0.13		[9]
ZIF-8	0.90	0.20	0.07		[10]
ZIF-8	0.67	0.22	0.13		[11]
ZIF-8	0.89	0.53	0.15	0.02	[12]
ZIF-8	0.83		0.09		[13]
ZIF-8	0.76	0.27	0.09		[14]
ZIF-8	0.70		0.07		[15]
ZIF-8	0.75		0.14		[16]
ZIF-8	0.73				[17]
ZIF-8	0.82	0.25	0.1		[18]
ZIF-8	0.46				[19]
ZIF-8	0.60		0.06		[20]
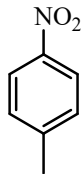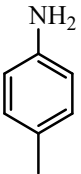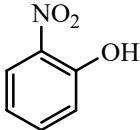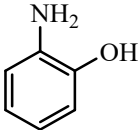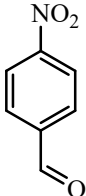
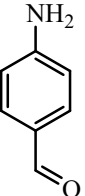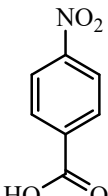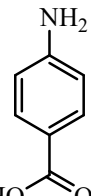|				
ZIF-8	0.85			[21]
ZIF-8	0.70	0.25		[22]

[a] The gas adsorption capacity was evaluated at 25 ^{o}C and 1 bar.

Table S3 Porous properties of Pd@HZIF-8 and Pd@SZIF-8

Samples	S_{BET} (m^2/g)	S_{meso}/S_{BET} (%)	V_{pore} (cm^3/g)	V_{meso}/V_{pore} (%)
Pd@HZIF-8	1341	25.5	1.07	67.7
Pd@SZIF-8	1627	1.9	0.63	7.9

Table S4 Catalytic performance of different catalysts for the hydrogenation of nitroarenes

Entry	Substrates	Catalysts	Con. (%)	Products
1[a]	NO_2 (4-nitrotoluene)	Pd@HZIF-8	93.4	NH_2 (4-methylaniline)
		Pd@SZIF-8	83.5	
2[b]	NO_2, OH (2-nitrophenol)	Pd@HZIF-8	100	NH_2, OH (2-aminophenol)
		Pd@SZIF-8	24.6	
3[c]	NO_2 (4-nitrobenzaldehyde)	Pd@HZIF-8	62.3	NH_2 (4-aminobenzaldehyde)
		Pd@SZIF-8	56.5	
4[d]	NO_2 (4-nitrobenzoic acid)	Pd@HZIF-8	71.0	NH_2 (4-aminobenzoic acid)
		Pd@SZIF-8	58.7	

[a] Reaction conditions: substrate 0.15 g, catalyst 0.015 g, NaBH$_4$ 0.2 g, water 10 mL, ethanol 10 mL, 30 °C, 5 min.

[b] Reaction conditions: substrate 0.1 g, catalyst 0.03 g, NaBH$_4$ 0.33 g, water 10 mL, ethanol 10 mL, 30 °C, 30 min.

[c] Reaction conditions: substrate 0.2 g, catalyst 0.01 g, NaBH$_4$ 0.1 g, water 10 mL, ethanol 10 mL, 30 °C, 20 min.

[d] Reaction conditions: substrate 0.15 g, catalyst 0.01 g, NaBH$_4$ 0.1 g, water 10 mL, ethanol 15 mL, 30 °C, 30 min.

Table S5 Pd loading of the catalysts

Samples	Pd loading (wt.%)
Pd@HZIF-8[a]	4.13
Pd@SZIF-8	0.82
Pd@HZIF-8[b]	3.78

[a] The theoretical Pd content is 4.3 wt.%.

[b] The recovered Pd@HZIF-8 after eight reaction cycles.

Table S6 Textural properties of HCNs

Samples	S_{BET} (m^2/g)	S_{meso} (m^2/g)	V_{total} (cm^3/g)	V_{meso} (cm^3/g)
HCN-0.6-6	338.6	153.1	0.411	0.345
HCN-1.2-6	411.2	248.0	0.511	0.431
HCN-2.4-6	400.3	181.4	0.470	0.353
HCN-3.6-6	492.4	223.2	0.570	0.459

Table S7 Element content in Pd@HCN catalysts

Samples	Co (wt.%)	Pd (wt.%)
Pd@HCN-0.6-6[a]	3.83	1.25
Pd@HCN-0.9-6[a]	3.74	1.38
Pd@HCN-1.2-6[a]	3.39	1.49
Pd@HCN-1.5-6[a]	3.82	1.39
Pd@HCN-2.4-6[a]	3.92	1.28
Pd@HCN-3.6-6[a]	3.68	1.37
Pd@HCN-1.2-6[b]	3.25	0.53
Pd@HCN-1.2-6[c]	3.57	2.83
Pd@HCN-1.2-6[d]	3.29	3.31

[a] The theoretical Pd content is 2 wt.%.

[b] The theoretical Pd content is 1 wt.%.

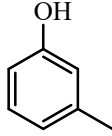[c] The theoretical Pd content is 3 wt.%.

[d] The theoretical Pd content is 4 wt.%.
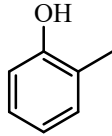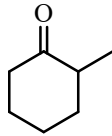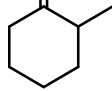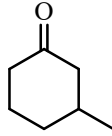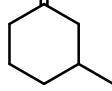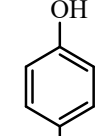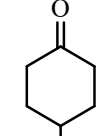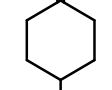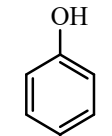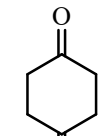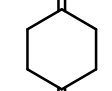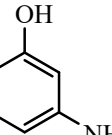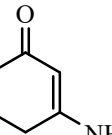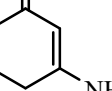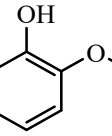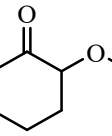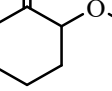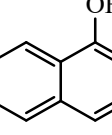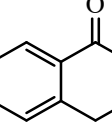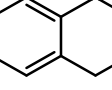
Table S8 Catalytic performance of various Pd-based catalysts applied to the phenol hydrogenation

Catalysts	$n_{Pd}:n_{phenol}$ (%)	Reaction conditions				Conversion (%)	Selectivity (%)	TOFs (h^{-1})	References
		Temperature (^{o}C)	Time (h)	Pressure (MPa)	Solvent				
Pd-chitin-150	4.2	90	2	0.1	Water	100	100	11.8	[23]
Pd/Z5(30)-33	1.5	25	24	0.1	Water	100	98	2.7	[24]
Pd/CeO$_2$	4.6	35	4	0.1	Hexane	94.1	90.8	4.6	[25]
Pd@CND	6.3	80	1	0.1	Water	96.9	94.1	14.5	[26]
[a]1Pd/HAP-SSD	5.0	85	1	0.1	Water	73.5	100	14.7	[27]
Na-Pd/TiO$_2$	0.4	80	6	0.1	Water	99	99	37.1	[28]
Pd(6.42%)/NCNs	4.8	80	4	0.1	Water	80	99	4.1	[29]
0.07-Pd/PNCM-800	10.0	80	3	0.1	Water	99	99.3	3.3	[30]
Pd@CN@TiO$_2$-8-450	3.2	80	1	0.1	Water	98	98.3	30.1	[31]
Pd/TNWs	0.5	50	5	0.5	Water	100	99	42.1	[32]
Pd@HMSNs	3.2	55	4	0.1	Water	99	98.3	7.6	[33]
Pd/pol-NH$_2$	5.0	100	4	0.1	Water	99.5	99.5	5.0	[34]
Pd@CN(1:3)-650	0.16	80	2	0.1	Cyclohexane	94	94.7	278.2	[35]

Pd@KL	0.8	60	11	1	Dichloromethane	99.2	94.8	11.1	[36]
ACN$_{pd}$	6.6	100	5	1	Dichloromethane	100	99.1	3.0	[37]
Pd@HCN-1.2-6	1.9	100	0.5	0.1	Cyclohexane	94.7	94.8	95.2	This work

TOFs are calculated by moles of cyclohexanone/ (moles of Pd*reaction time).

Table S9 Catalytic performance of different catalysts for the hydrogenation of phenol derivatives

Entry	Substrates	Catalysts	Con. (%)	Major products	Sel. (%)
1[a]		Pd@HCN-1.2-6	49.7		97.4
		Pd@HCN-2.4-6	38.9		96.4
2[a]		Pd@HCN-1.2-6	63.6		92.3
		Pd@HCN-2.4-6	52.2		97.4
3[a]		Pd@HCN-1.2-6	89.3		91.7
		Pd@HCN-2.4-6	75.5		95.6
4[b]		Pd@HCN-1.2-6	100		30.1
		Pd@HCN-2.4-6	100		17.0
5[b]		Pd@HCN-1.2-6	94.3		97.0
		Pd@HCN-2.4-6	79.7		97.9
6[c]		Pd@HCN-1.2-6	73.2		52.8
		Pd@HCN-2.4-6	52.8		49.0
7[b]		Pd@HCN-1.2-6	63.0		94.3
		Pd@HCN-2.4-6	56.1		91.3

[a] Reaction conditions: 1 wt. % substrate cyclohexane solution 5 mL, catalyst 0.03 g, 0.1 MPa H_2, 2.8 wt.% Pd, 100 °C, 60 min.

[b] Reaction conditions: 1 wt. % substrate water solution 5 mL, catalyst 0.03 g, 0.1 MPa H_2, 2.8 wt.%

Pd, 80 °C, 30 min.

[c] Reaction conditions: 1 wt. % substrate water solution 5 mL, catalyst 0.03 g, 0.1 MPa H_2, 2.8 wt.%

Pd, 80 °C, 720 min.

References

1. J. Zhang, Z. Low, Y. Shao, H. Jiang and R. Chen, *Chem. Commun.*, 2022, **58**, 1422-1425.

2. C. Rösler, A. Aijaz, S. Turner, M. Filippousi, A. Shahabi, W. Xia, G. Van Tendeloo, M. Muhle and R. A. Fischer, *Chem. Eur. J.*, 2016, **22**, 3304-3311.

3. Y. Wang, B. Wang, H. Yuan, Z. Liang, Z. Huang, Y. Zhou, W. Zhang, H. Zheng and R. Cao, *J. Energy Chem.*, 2021, **58**, 391-396.

4. F. Şahin, B. Topuz and H. Kalıpçılar, *Microporous Mesoporous Mater.*, 2018, **261**, 259-267.

5. R. Chen, J. Yao, Q. Gu, S. Smeets, C. Baerlocher, H. Gu, D. Zhu, W. Morris, O. M. Yaghi and H. Wang, *Chem. Commun.*, 2013, **49**, 9500-9502.

6. G. Xu, J. Yao, K. Wang, L. He, P. A. Webley, C.. Chen and H. Wang, *J. Membr. Sci.*, 2011, **385-386**, 187-193.

7. M. Zeeshan, H. Kulak, S. Kavak, H. M. Polat, O. Durak, S. Keskin and A. Uzun, *Microporous Mesoporous Mater.*, 2020, **306**, 110446.

8. C. Jiao, Z. Li, X. Li, M. Wu and H. Jiang, *Sep. Purif. Technol.*, 2021, **259**, 118190.

9. K. Y. Cho, H. An, X. H. Do, K. Choi, H. G. Yoon, H. Jeong, J. S. Lee and K. Baek, *J. Mater. Chem. A*, 2018, **6**, 18912-18919.

10. C. Kong, H. Du, L. Chen and B. Chen, *Energy Environ. Sci.*, 2017, **10**, 1812-1819.

11. M. Zeeshan, S. Keskin and A. Uzun, *Polyhedron*, 2018, **155**, 485-492.

12. S. Liu, W. Li and J. Zhang, *New J. Chem.*, 2020, **44**, 95-101.

13. F. Yang, T. Ge, X. Zhu, J. Wu and R. Wang, *Sep. Purif. Technol.*, 2022, **287**, 120535.

14. F. P. Kinik, C. Altintas, V. Balci, B. Koyuturk, A. Uzun and S. Keskin, *ACS Appl. Mater. Interfaces*, 2016, **8**, 30992-31005.

15. S. Gadipelli, W. Travis, W. Zhou and Z. Guo, *Energy Environ. Sci.*, 2014, **7**, 2232-2238.

16. S. Xian, F. Xu, C. Ma, Y. Wu, Q. Xia, H. Wang and Z. Li, *Chem. Eng. J.*, 2015, **280**, 363-369.

17. M. Thomas, B. N. Nair, G. M. Anilkumar, A. P. Mohamed, K. G. K. Warrier and U. S. Hareesh, *J. Environ. Chem. Eng.*, 2016, **4**, 1442-1450.

18. J. McEwen, J. Hayman and A. Ozgur Yazaydin, *Chem. Phys.*, 2013, **412**, 72-76.

19. M. Du, L. Li, M. Li and R. Si, *RSC Adv.*, 2016, **6**, 62705-62716.

20. S. Zhong, Q. Wang and D. Cao, *Sci. Rep.*, 2016, **6**, 21295.

21. M. Fan, F. Gai, Y. Cao, Z. Zhao, Y. Ao, Y. Liu and Q. Huo, *J. Solid State Chem.*, 2019, **269**, 507-512.

22. L. H. Wee, S. Vandenbrande, S. M. J. Rogge, J. Wieme, K. Asselman, E. O. Jardim, J. Silvestre-Albero, J. A. R. Navarro, V. Van Speybroeck, J. A. Martens and C. E. A. Kirschhock, *J. Am. Chem. Soc.*, 2021, **143**, 4962-4968.

23. C. Zhao, Z. Zhang, Y. Liu, N. Shang, H.-J. Wang, C. Wang and Y. Gao, *ACS Sustainable Chem. Eng.*, 2020, **8**, 12304-12312.

24. A. Chang, T. Yang, M. Chen, H. Hsiao and C. Yang, *J. Hazard. Mater.*, 2020, **400**, 123241.

25. N. C. Nelson, J. S. Manzano, A. D. Sadow, S. H. Overbury and I. I. Slowing, *ACS Catal.*, 2015, **5**, 2051-2061.

26. S. Ding, C. Zhang, Y. Liu, H. Jiang and R. Chen, *Appl. Surf. Sci.*, 2017, **425**, 484-491.

27. Y. Shen, X. Bo, Z. Tian, Y. Wang, X. Guo, M. Xie, F. Gao, M. Lin, X. Guo and W. Ding, *Green Chem.*, 2017, **19**, 2646-2652.

28. H. Zhou, B. Han, T. Liu, X. Zhong, G. Zhuang and J. Wang, *Green Chem.*, 2017, **19**, 3585-

3594.

29. M. Fan, Y. Long, Y. Zhu, X. Hu and Z. Dong, *Appl. Catal., A*, 2018, **568**, 130-138.

30. Y. Zhu, G. Yu, J. Yang, M. Yuan, D. Xu and Z. Dong, *J. Colloid Interface Sci.*, 2019, **533**, 259-267.

31. J. Zhang, H. Jiang, Y. Liu and R. Chen, *Appl. Surf. Sci.*, 2019, **488**, 555-564.

32. C. Tian, H. Fang, H. Chen, W. Chen, S. Zhou, X. Duan, X. Liu and Y. Yuan, *Nanoscale*, 2020, **12**, 2603-2612.

33. C. Yang, K. Li, J. Wang and S. Zhou, *Appl. Catal., A*, 2021, **610**, 117961.

34. S. Xu, J. Du, Q. Zhou, H. Li, C. Wang and J. Tang, *J. Colloid Interface Sci.*, 2021, **604**, 876-884.

35. J. Zhang, Z. X. Low, Y. Shao, H. Jiang and R. Chen, *Chem. Commun.*, 2022, **58**, 1422-1425.

36. C. Liu, J. Wang, P. Zhu, H. Liu and X. Zhang, *Chem. Eng. J.*, 2022, **430**, 132589.

37. Q. Wu, L. Wang, B. Zhao, L. Huang, S. Yu and A. J. Ragauskas, *J. Colloid Interface Sci.*, 2022, **605**, 82-90.